

## 1065 CHAPTER 5

# 1066 RESULTS

1067 In chapter 4, all the ingredients to calculate the antiproton to proton flux ratio are given. In this  
1068 chapter, the calculated antiproton to proton flux ratio in time averaged and time dependent analysis  
1069 is shown.

### 1070 5.1. Time Averaged Result

1071 In August 2016, the AMS-02 collaboration published the time-averaged antiproton to proton flux  
1072 ratio up to 450 GV with four years data (taken from May 2011 to May 2015). In Feb 2021, the AMS-  
1073 02 collaboration published the flux ratio up to 525 GV with six and half years data. Nowadays, the  
1074 data has been taken continuously up to May 2021, and this analysis is based on the latest ten years  
1075 data. With more data, the antiproton to proton flux ratio can be updated with higher statistics and  
1076 improved accuracy.

1077 Since the antiproton to proton flux ratio is determined in three different ranges, the time-averaged  
1078 antiproton to proton flux ratio is given in figure 5.1 with the overlapping range. The results in the  
1079 overlapping range are consistent with each other. In figure 5.2, the final antiproton to proton flux  
1080 ratio in this analysis is shown.

1081 In the highest rigidity range, the antiproton to proton ratio shows a relatively flat trend. No obvious  
1082 falling trend is observed as the positron to electron flux ratio shown in the latest paper from AMS-02  
1083 collaboration [107] . To observe the behavior in a higher rigidity range, more data is required and  
1084 better charge confusion separation is needed.

1085 To check the consistency between the result in this analysis and in AMS-02 published result in Physics  
1086 Report [107] , the same data period is used. In figure 5.3, the antiproton to proton flux ratios in  
1087 this analysis based on six and half years data is shown. Compared with the result in Physics Report  
1088 based on the same data period, the result in this analysis, as an independent analysis, matches well  
1089 within the error bars.

1090 The total error breakdown is shown in 5.4. In the high rigidity range, the error is mainly domi-  
1091 nated by systematic error due to the dominant background of charge confused protons and limited

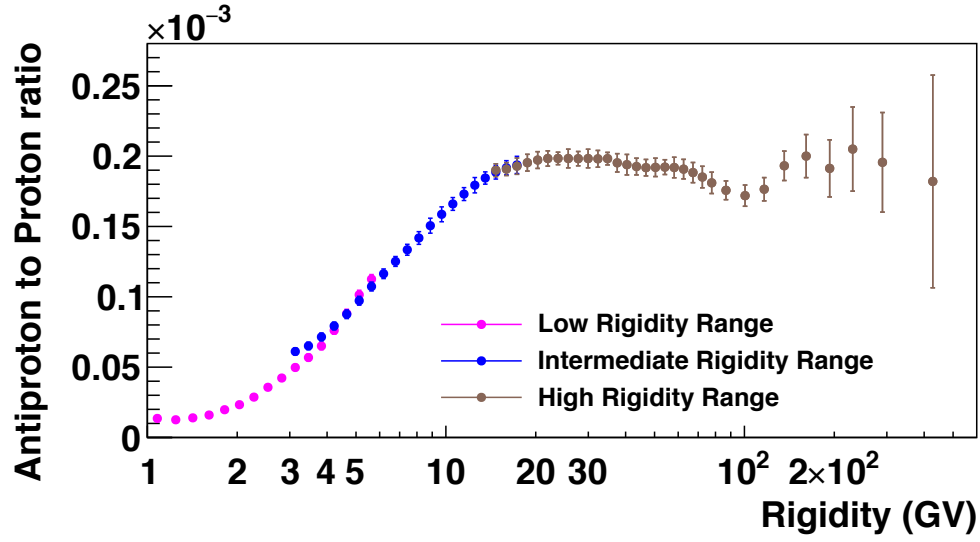


Figure 5.1: The time-averaged antiproton to proton flux ratios in three rigidity ranges is shown. In the overlapping ranges, the results from different template fit methods are consistent with each other. The error bars are total errors calculated from the quadratic sum of statistical and systematic errors.

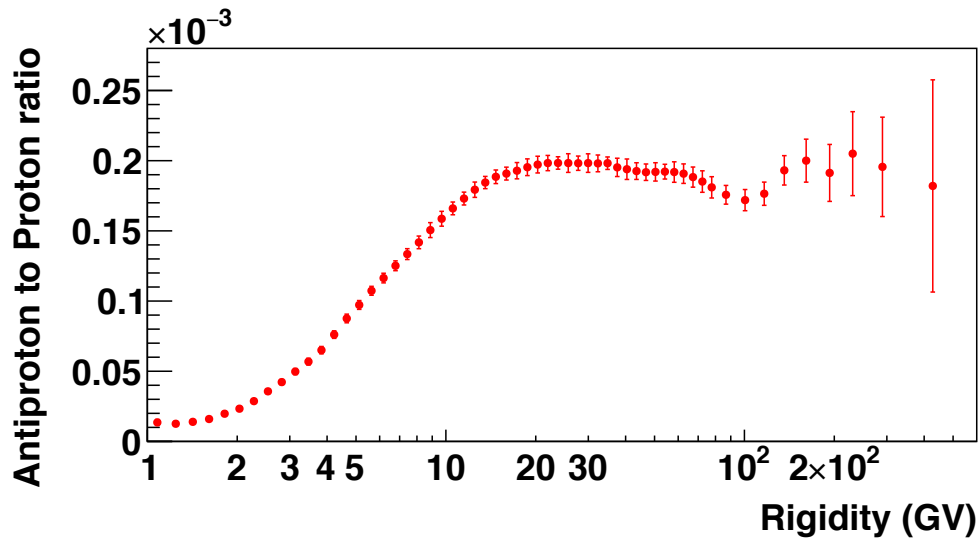


Figure 5.2: The final result of the time-averaged antiproton to proton flux ratio with the data taken from May 2011 to May 2021 in this analysis. The error bar is the total error calculated from the quadratic sum of statistical and systematic error.

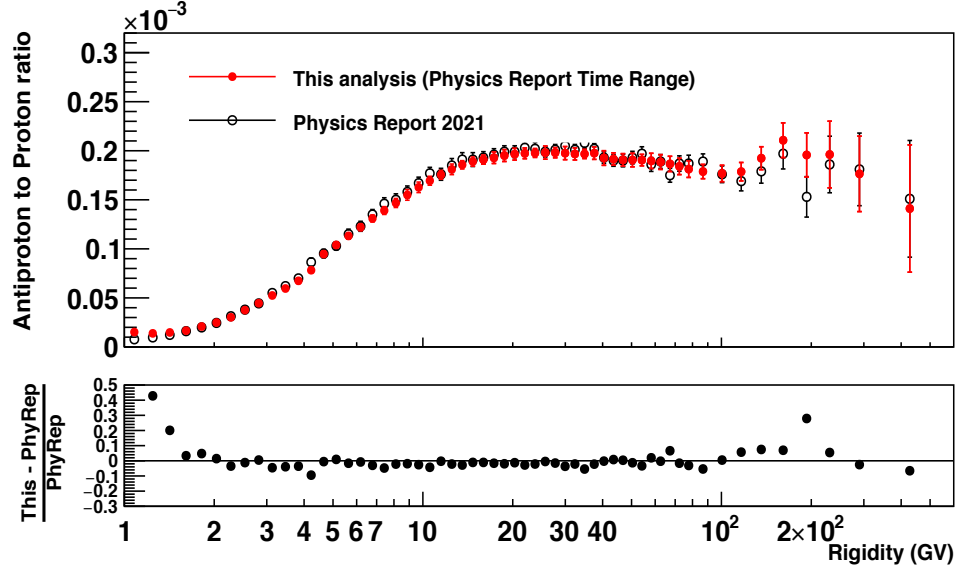


Figure 5.3: Comparison between the antiproton to proton flux ratio in this analysis and in Physics Report [107] , both of the two flux ratios use six and half years of data. The two results match with each other within the error bars.

1092 separation power. In the intermediate range, the error is dominated by systematic error due to  
 1093 the effective acceptance. In the lowest rigidity range, namely below 2 GV, the contributions from  
 1094 statistical and systematic error are at a similar level, which is much improved from the previous  
 1095 antiproton publication with four years data collected.

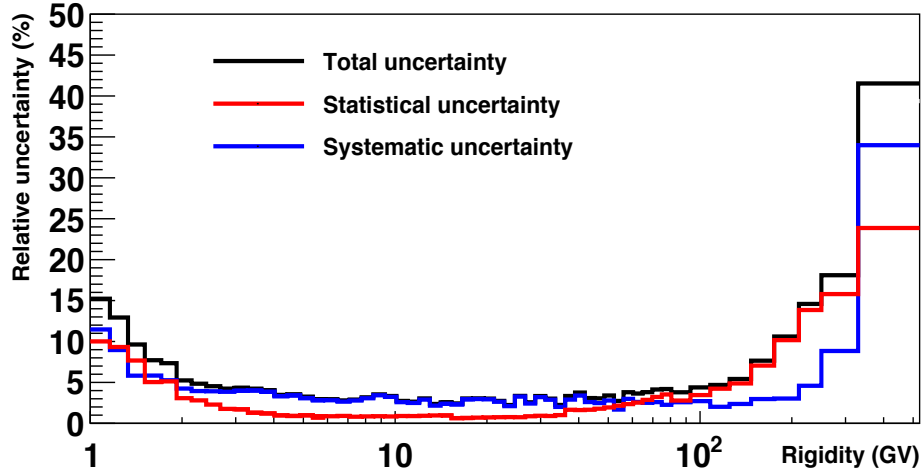


Figure 5.4: The uncertainty breakdown of the time-averaged antiproton to proton flux ratio in this analysis. In the highest rigidity bin, the systematic uncertainty is dominated due to the charge confusion protons. In the low rigidity range, the statistical uncertainty and systematic uncertainty make similar contributions.

## 1096 5.2. Time Dependent Result

1097 Apart from the time-averaged antiproton to proton flux ratio, the time-dependent antiproton to  
 1098 proton flux ratio can also be calculated with the same strategy. For the time-dependent analysis,  
 1099 the antiproton to proton flux ratio is determined in six Bartels Rotations. In total, 14 time-dependent  
 1100 antiproton to proton flux ratios are obtained from 1.16 GV to 18 GV. The time-dependent antiproton  
 1101 to proton flux ratio is given in 5.5. In this figure, the variation caused by solar modulation is clearly  
 1102 shown.

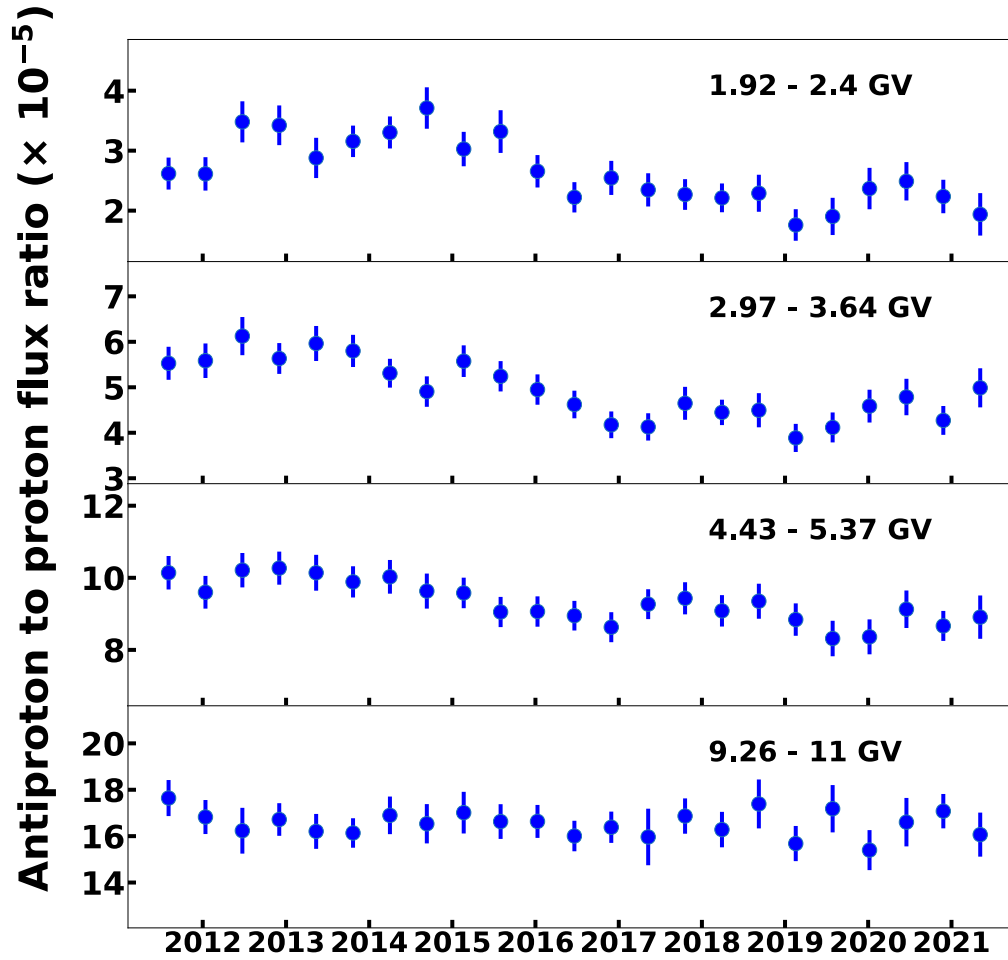


Figure 5.5: Time-dependent antiproton to proton flux ratios for four of the 14 rigidity bins. The error bars in this figure are total errors, including statistical errors and systematic errors. Distinct time variation structures are visible in these ratios.

One important observation is that with the rigidity going up, the solar modulation effect is weaker. In the first rigidity bin in this figure, the flux ratio changes by a factor 2 between its minimum and maximum, while in the last one, the fluctuation only changes around 20%. Above 15 GV, the modulation effect is ignorable, and the fluctuation is mainly dominated by noise.

In general, the antiproton to proton flux ratio shows a rising trend up to around 2014, then gradually going down up to the beginning of 2017. After 2017, the flux ratio is relatively flat but slowly rising.

Apart from the long-time trend, there are few fine time structures like around the beginning of 2013, the ratio fell quickly and then recovered soon. Those fine time structures need to be studied in detail with fine time bins.

For illustration, the total error breakdown in an example rigidity bin of 1.92 - 2.4 GV is shown in 5.6. Because of the limited statistics in six Bartels Rotations, the statistical error is dominant in time-dependent results.

In 5.7, the statistical error contributions in total error in 1.92- 2.4 GV is shown, and the statistical error shows a relatively rising trend from 60% to almost 80%.

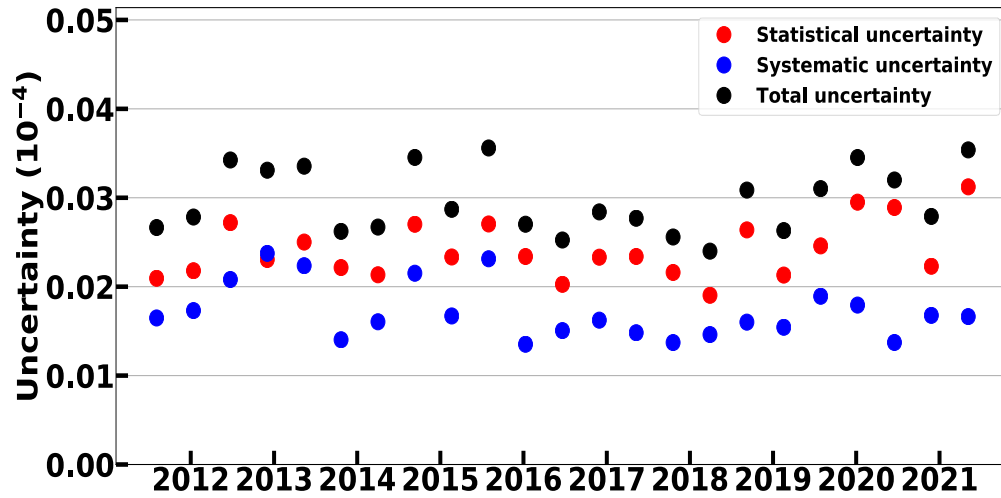


Figure 5.6: Breakdown of the total uncertainty of the antiproton to proton flux ratio into a statistical and systematical part in 1.92 to 2.4 GV.

In figure 5.8, the time-averaged antiproton to proton flux ratio and the 23 time-dependent antiproton to proton flux ratios are shown. The time-dependent antiproton to proton flux ratios have some time-dependent variations but mainly fluctuate around the time-averaged antiproton to proton flux ratio.

To compare further between the time-averaged and dependent antiproton to proton flux ratio, the

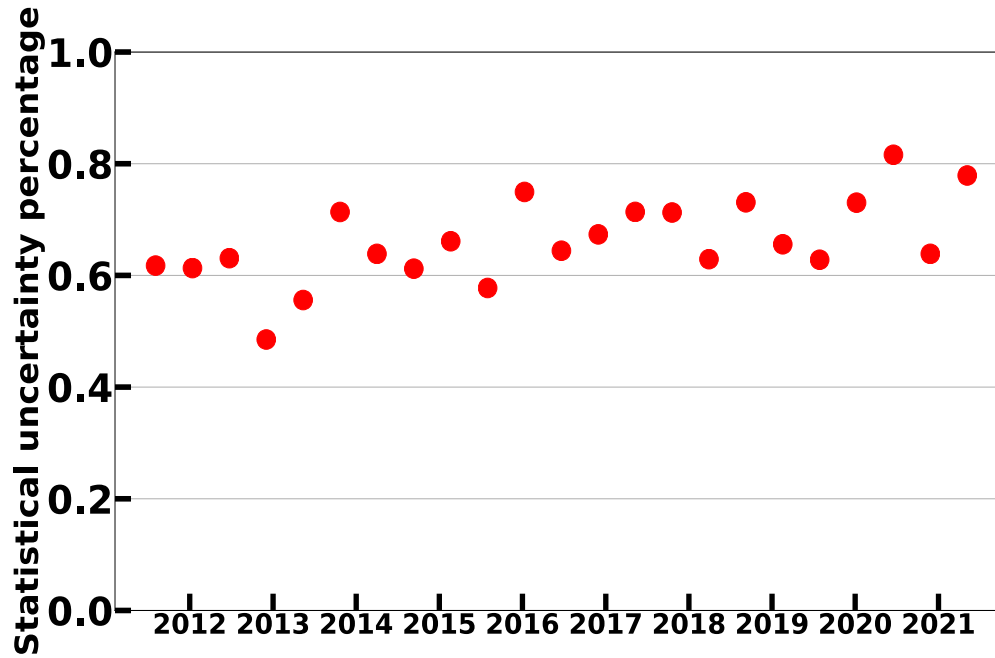


Figure 5.7: Percentage of statistical uncertainty in total uncertainty of the antiproton to proton flux ratio in 1.92 - 2.4 GV.

1122 merging of the time-dependent numbers is done. In each rigidity bin, the 23 time-dependent antipro-  
 1123 ton numbers and proton numbers are merged respectively. Then the merged antiproton to proton  
 1124 flux ratios is constructed.

1125 In figure 5.9, the time-averaged antiproton to proton flux ratio and the merged antiproton to proton  
 1126 flux ratio are shown. From this comparison, the merged time-dependent antiproton to proton flux  
 1127 ratio match well with the time-averaged antiproton to proton flux ratio, while in the first few bins,  
 1128 the merged antiproton to proton flux ratio deviates a little due to the low statistics.

1129 Since the solar variation affects all kinds of cosmic rays, the obtained time-dependent antiproton  
 1130 to proton flux ratio can be compared with other results. In figure 5.10, the antiproton to proton  
 1131 flux ratio in this analysis is shown together with the electron to positron flux ratio. The electron to  
 1132 positron flux ratio is taken from [103], and the result is consistent with previous AMS-02 publication  
 1133 in [48] but with a data extension. The electron to positron flux ratio is presented in its ECAL  
 1134 energy bins. To compare in the exact same rigidity bin as used for antiproton to proton flux ratio,  
 1135 the electron and positron fluxes are fitted with a power-law modulated according to the force-field  
 1136 approximation, then integrated the electron and positron fluxes over the rigidity bin used for the  
 1137 antiproton to proton flux ratio, at last, the electron to positron flux ratio in antiproton to proton  
 1138 flux ratio bins can be obtained. Due to the charge sign difference, the two flux ratios are shown in  
 1139 negative charge particles over positive charge particles. The normalization of electron to positron  
 1140 flux ratio is based on the first two years data to make sure the mean of electron to positron flux

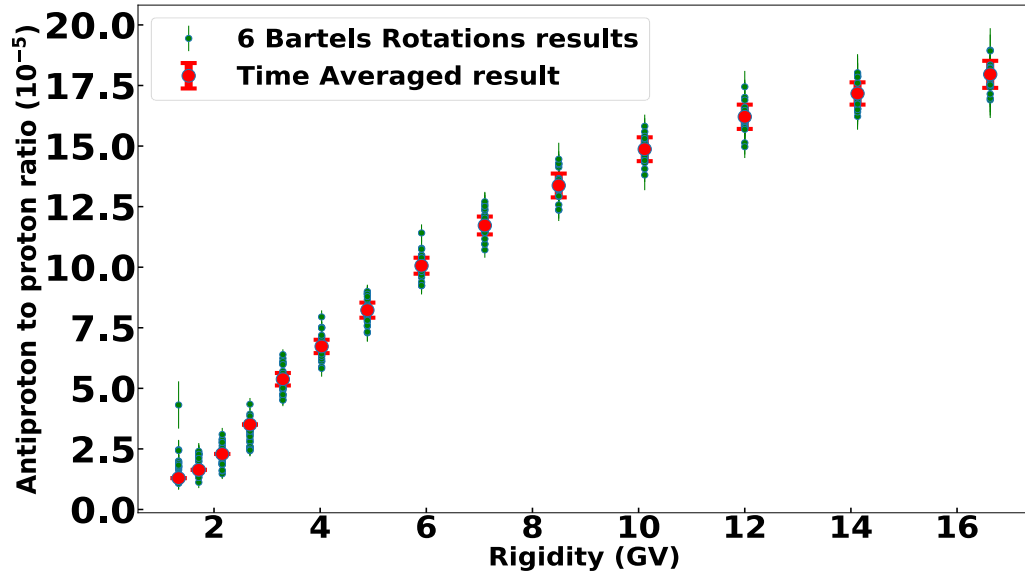


Figure 5.8: time-averaged antiproton to proton flux ratio (red) and 23 time-dependent antiproton to proton flux ratios in six Bartels rotations (green). The time-dependent results are changed around the time-averaged result.

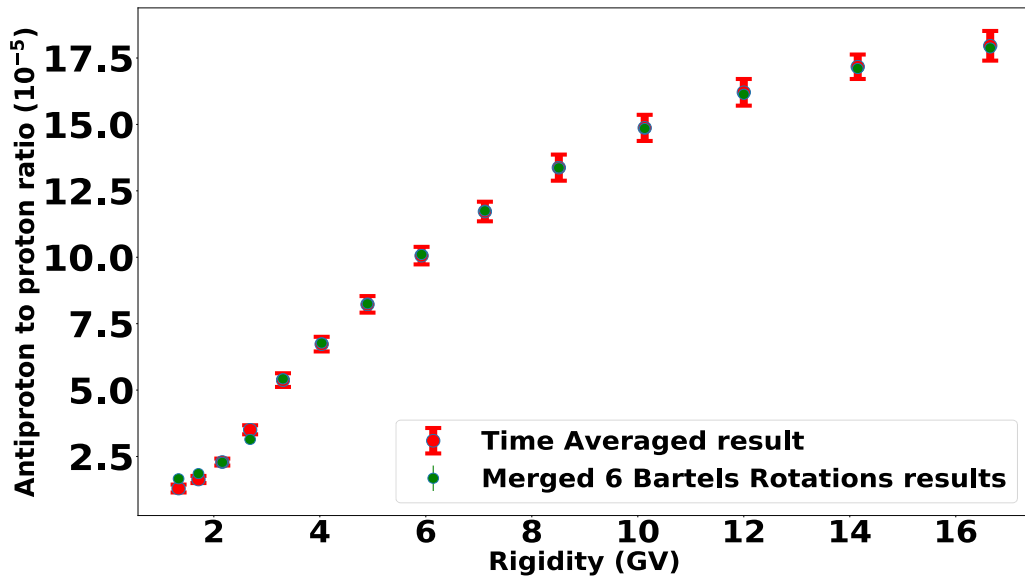


Figure 5.9: Time-averaged antiproton to proton flux ratio (red) and merged time-dependent antiproton to proton flux ratios in six Bartels rotations (green). The merged time-dependent result matches well with the time-averaged result.

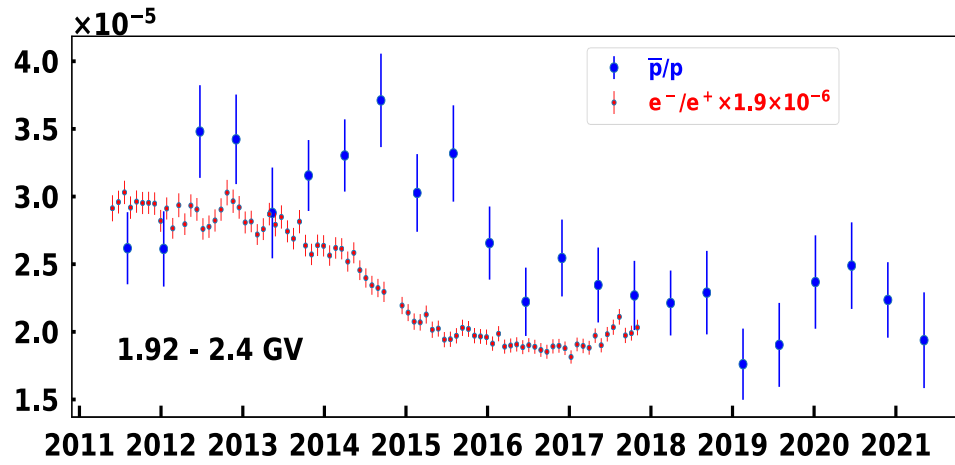
1141 ratio is the same as the mean of the antiproton to proton flux ratio.

1142 By comparing the antiproton to proton flux ratio and electron to positron flux ratio, the first  
1143 observation is the time variation effects in both flux ratios are decreasing with rigidity going up and  
1144 this observation is expected.

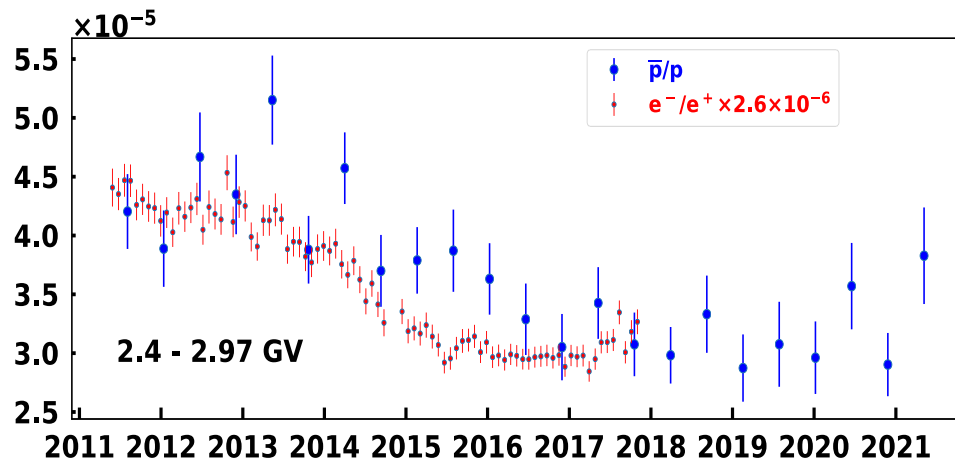
1145 The second observation is the time variation trend of the antiproton to proton flux ratio is different  
1146 from the electron to positron flux ratio in the low rigidity range. For example, below 3 GV, both  
1147 ratios go up first and then drop down to the minimum, at last gradually rebound. While the  
1148 antiproton to proton flux ratio seems to have a delay than the electron to positron flux ratio. This  
1149 difference gradually gone with the rigidity going up, and the trend of the two ratios become similar  
1150 in rigidity higher than 6 GV.

1151 For solar modulation modeling, the Local Interstellar Spectra (LIS) are important inputs. The LIS  
1152 of antiproton and positron are different [108] . Therefore, this could lead to a difference between  
1153 antiproton to proton flux ratio trend and electron to positron flux ratio trend. Another important  
1154 difference is the mass difference. Antiproton and proton have much larger mass than electron and  
1155 positron. This difference has much impact in the lower rigidity range. So, both two reasons could  
1156 result in different flux ratios in the low rigidity range.

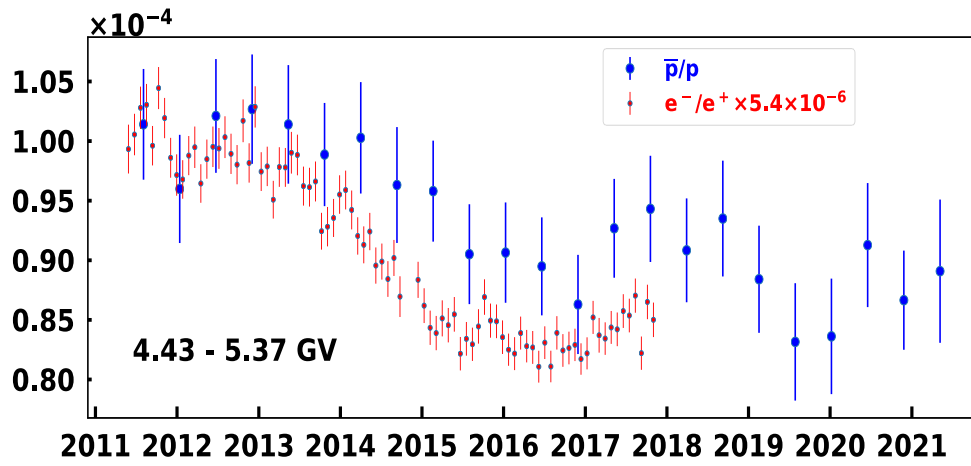




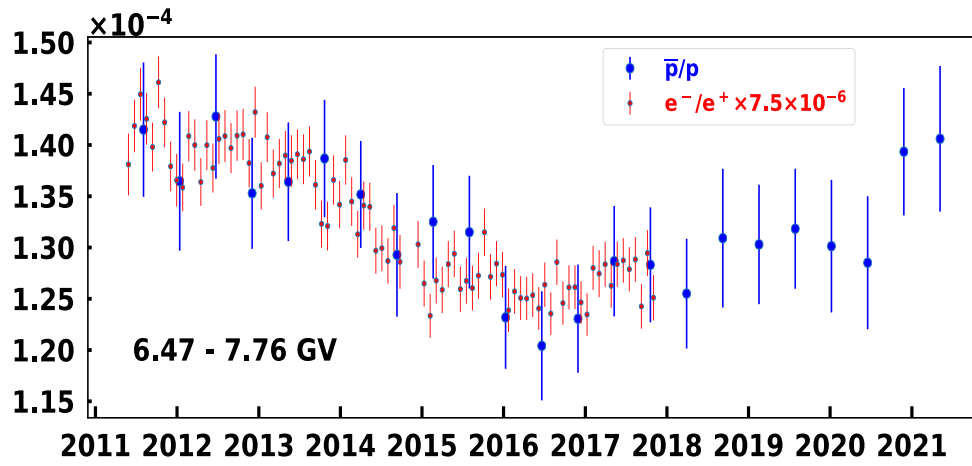
(a)



(b)



(c)



(d)

Figure 5.10: Comparison between antiproton to proton flux ratio (blue) and electron to positron flux ratio (red) in four rigidity bins: a). 1.92-2.4 GV b). 2.4-2.97 GV c). 4.43-5.37 GV d). 6.47-7.76 GV. The error bars are the total errors calculated from the quadratic sum of statistical errors and systematic errors.

## 1157 CHAPTER 6

## 1158 SUMMARY

1159 In the thesis, the time-averaged antiproton to proton flux ratio is presented up to 525 GV with  
1160 ten years of AMS-02 cosmic rays data, which is the highest and most accurate measurement up  
1161 to date. The unprecedented accuracy provides a probe for us to understand the origin of cosmic  
1162 ray antiprotons. The antiproton to proton flux ratio in the high rigidity range shows a flat trend  
1163 in previous AMS-02 publication with four years data [1] , instead of a falling trend predicted by  
1164 secondary production models [26, 27] . This observation doesn't change in this analysis result with  
1165 the latest ten years data. This analysis is an independent result of the AMS-02 Physics Report  
1166 result in [107] , which also presents the antiproton to proton flux ratio up to 525 GV.

1167 Except the time-averaged antiproton to proton flux ratio, the time-dependent antiproton to proton  
1168 flux ratio in every six Bartels Rotations data is presented in this thesis. From 1.16 GV to 18 GV,  
1169 the time-dependent antiproton to proton flux ratios are given in 14 rigidity bins. The rigidity bins  
1170 are merged in every two rigidity bins in time-averaged analysis to increase the statistics.

1171 The first observation is that with rigidity going up, the solar modulation effect is weaker. The  
1172 antiproton to proton flux ratio shows a distinct time structure up to around 15 GV. The data is  
1173 taken from May 2011 to May 2021, which covers eight years in solar cycle 24 and two years in solar  
1174 cycle 25. In this period, the behavior of the antiproton to proton flux ratio shows a rising trend first  
1175 and going down to the minimum, at last gradually going up. This behavior can be used to compare  
1176 and check with solar modulation models [109, 108] .

1177 The second observation is from the comparison between the antiproton to proton flux ratio and the  
1178 electron to positron flux ratio. The antiproton to proton flux ratio is different from the electron to  
1179 positron flux ratio below 3 GV, and this difference gradually gone with rigidity going up. Above 6  
1180 GV, this difference almost disappears and the two flux ratios show a similar trend. The different  
1181 behaviors could be due to the different LIS of antiprotons and positrons in the low rigidity range,  
1182 therefore they are subject to different modulation results. In addition, the mass difference between  
1183 antiproton (proton) and positron (electron) also plays important role in the low rigidity range.

1184 AMS-02 will continue to collect data until the lifetime of ISS, which is estimated to be 2030. The  
1185 improved statistics will reduce the statistical error further in the high rigidity range and give a more

1186 precise measurement. For time-dependent analysis, the time variation effect on the antiproton to  
1187 proton flux ratio has already been shown in ten years period in this work. With the data collected  
1188 in the future, the time variation effect in the complete 11 years solar cycle can be obtained. On the  
1189 other hand, the antiproton to proton flux ratio in six Bartels Rotations time resolution shows the  
1190 time structure in the long time period, the observation of fine time structure requires higher time  
1191 resolutions. To achieve this, improved analysis method with higher statistics in each time-dependent  
1192 period allows a stable result in finer time resolution.

1193 After the AMS-02 experiment, a next-generation magnetic spectrometer in space called AMS-100  
1194 is in progress [\[110\]](#) , which will be placed on the Lagrange point L2 in around 2039. The AMS-100  
1195 can provide  $100\text{ m}^2\text{sr}$  acceptance and allow a measurement of the antiproton to proton flux ratio  
1196 up to 10 TV. For the time-dependent analysis, the AMS-100 can continue the study of the solar  
1197 modulation on the cosmic antiprotons for decades.

# APPENDIX

## Input variables for charge confusion

Except for the four variables shown in section 4.2, the full list of the 12 left input variables used in the training charge confusion estimator is given in this appendix. Nine of them are constructed from the Tracker, two of them are constructed from the TOF, and one of them is constructed from the TRD.

### 1. Rigidity Asymmetry and Matching

The rigidity is constructed from the Tracker. With the different tracker layers, different rigidity values are obtained. Therefore, the asymmetry and matching variables can be constructed further and used as the inputs of training. Two variables related to this are used: RigidityAsymmetryL9 and L24L58RigidityMatching. The definitions are given below:

$$\begin{aligned} \text{RigidityAsymmetryL9} &= \frac{\text{RigidityInnerL9} - \text{RigidityInner}}{\text{RigidityInnerL9} + \text{RigidityInner}} \\ \text{L24L58RigidityMatching} &= \left[ \left( \frac{1.0}{\text{RigidityInnerUpper}} \right) - \left( \frac{1.0}{\text{RigidityInnerLower}} \right) \right] \cdot \frac{100R}{|R|} \end{aligned}$$

where the RigidityInner and RigidityInnerL9 are the rigidities constructed from the inner tracker layer and the inner tracker layer plus layer 9, RigidityInnerUpper and RigidityInnerLower are constructed from the upper half of the inner tracker layer and the lower half of the inner tracker layer.

In figure 1, the distributions of the two variables are shown.

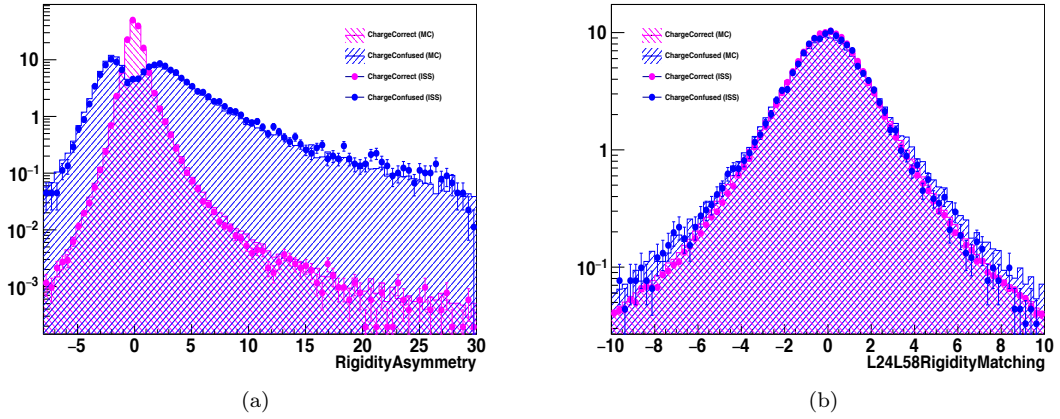


Figure 1: Distributions of a). RigidityAsymmetry b). L24L58RigidityMatching in example rigidity bin of 330 to 525 GV. Histograms (magenta: charge correct; blue: charge confused) are taken from MC and points (magenta: charge correct; blue: charge confused) are from data.

## 1214 2. Tracker Fit Chi2

1215 The tracker track fit quality provides important information for charge confusion. Due to the  
 1216 interaction, the poorer fit quality, the more likely to be charge confused event. Therefore, the  
 1217 fit Chi2 could be used as the input for training. In total, four variables related to Chi2 are used:  
 1218 Log10Chi2TrackerX and Log10Chi2TrackerY are the tracker track fit Chi2 in logarithmic on  
 1219 X and Y sides respectively. Log10Chi2TrackerXInner and Log10Chi2TrackerYInner are the  
 1220 inner tracker track fit Chi2 in logarithmic on X and Y sides respectively. In figure 2, the  
 1221 distributions of these four variables are shown.

## 1222 3. Tracker Charge

1223 Due to the interaction, the tracker charge measurement at the lower part could be contami-  
 1224 nated. Therefore, this information could be added to the training variable list. The Track-  
 1225 erL9Charge and TrackerL78Charge are the two variables related to this. TrackerL9Charge  
 1226 is the tracker charge measurement from layer 9. TrackerL78Charge is the mean value of the  
 1227 tracker charge measurement from layer 7 and 8. In figure 3, the distributions of the two  
 1228 variables are shown.

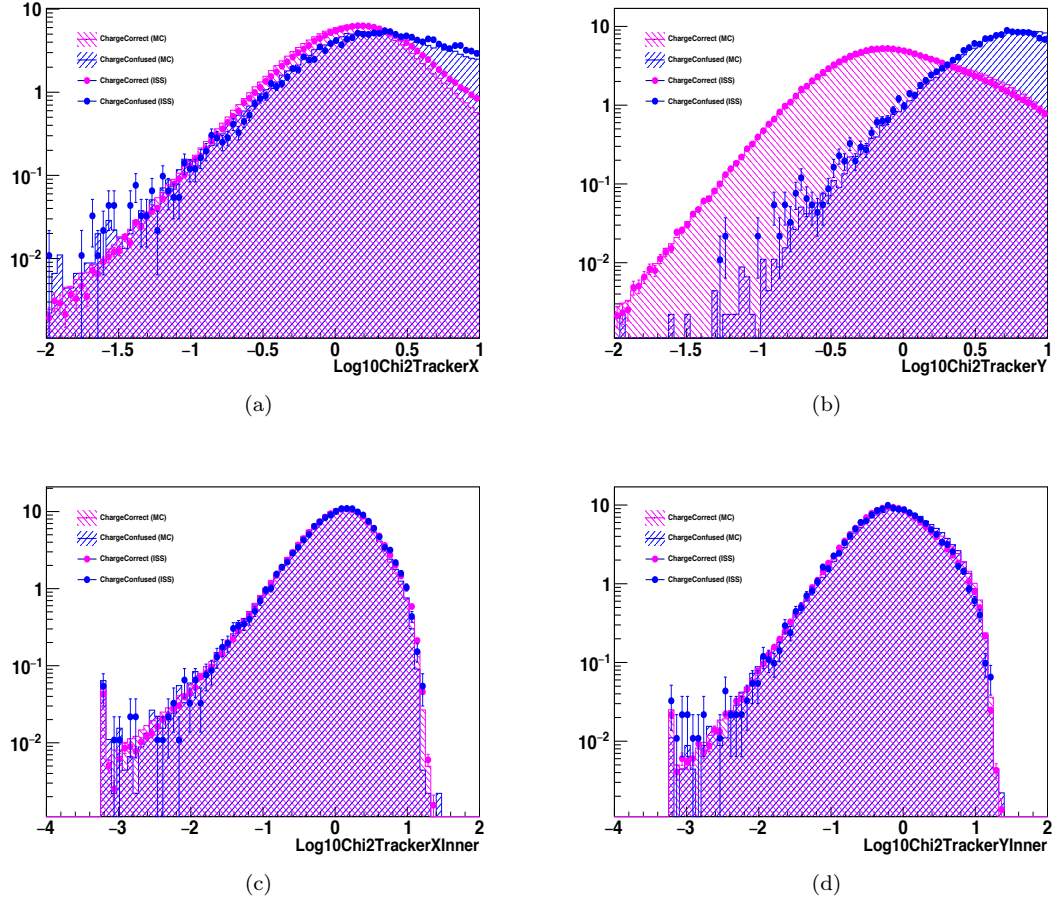


Figure 2: Distributions of a).  $\text{Log}_{10}\text{Chi2TrackerX}$  b).  $\text{Log}_{10}\text{Chi2TrackerY}$  c).  $\text{Log}_{10}\text{Chi2TrackerXInner}$  d).  $\text{Log}_{10}\text{Chi2TrackerYInner}$  in example rigidity bin of 330 to 525 GV. Histograms (magenta: charge correct; blue: charge confused) are taken from MC and points (magenta: charge correct; blue: charge confused) are from data.

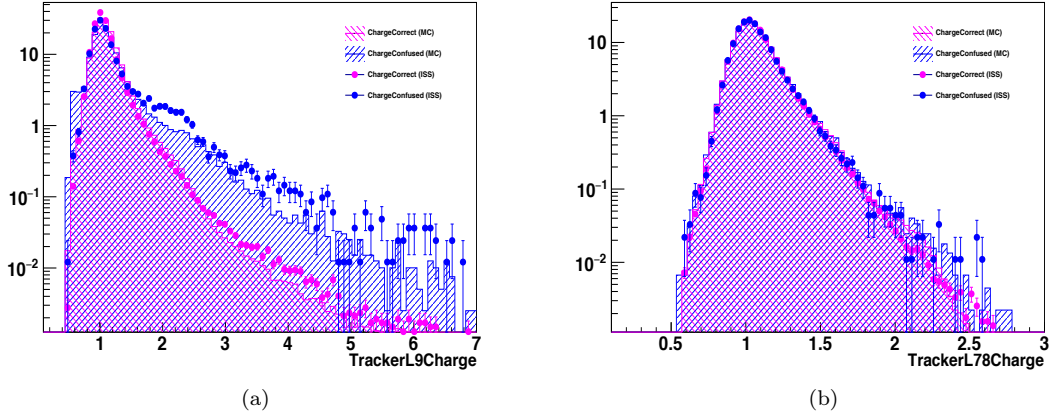


Figure 3: Distributions of a). TrackerL9Charge b). TrackerL78Charge in example rigidity bin of 330 to 525 GV. Histograms (magenta: charge correct; blue: charge confused) are taken from MC and points (magenta: charge correct; blue: charge confused) are from data.

#### 4. Charge Asymmetry

The tracker charge asymmetry also provides information about charge confusion. TrackerL58L24ChargeAsymmetry is the asymmetry of tracker charge measurements and its definition is given below:

$$\text{TrackerL58L24ChargeAsymmetry} = \frac{\text{TrackerL58Charge} - \text{TrackerL24Charge}}{\text{InnerTrackerCharge}}$$

where the TrackerL58Charge is the mean value of the tracker charge from layer 5 and 8. TrackerL24Charge is the mean value of the tracker charge from layer 2 and 4. InnerTrackerCharge is the tracker charge from the inner tracker.

In figure 4, the distributions of the TrackerL58L24ChargeAsymmetry is shown.

#### 5. TOF Charge

Except the tracker charge, the charge measurements from the TOF also are used in training. UpperTofCharge and LowerTofCharge are the TOF charge measurements from upper TOF and lower TOF. In figure 5, the distributions of the UpperTofCharge and LowerTofCharge are shown.



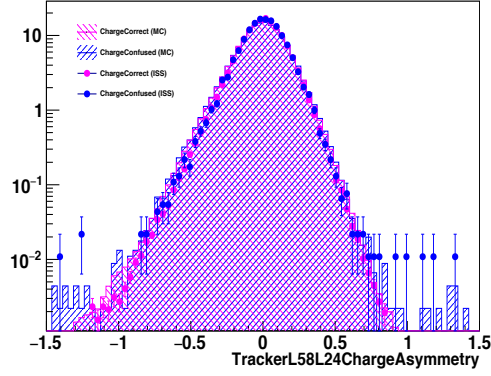


Figure 4: Distributions of TrackerL58L24ChargeAsymmetry in example rigidity bin of 330 to 525 GV. Histograms (magenta: charge correct; blue: charge confused) are taken from MC and points (magenta: charge correct; blue: charge confused) are from data.

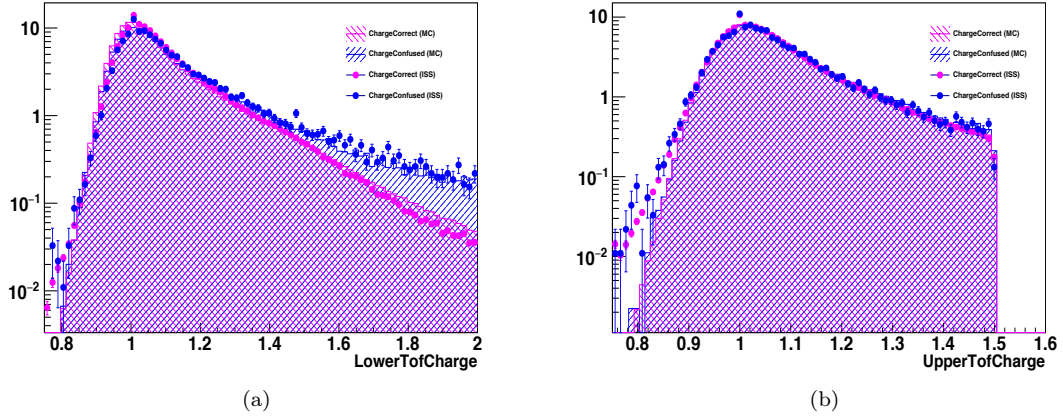


Figure 5: Distributions of a). LowerTofCharge b). UpperTofCharge in example rigidity bin of 330 to 525 GV. Histograms (magenta: charge correct; blue: charge confused) are taken from MC and points (magenta: charge correct; blue: charge confused) are from data.

## 1242 6. TRDLikelihood

1243 The last variable is the TRDLikelihood. Because of the potential interactions in the TRD for  
 1244 charge confused events, the TRDLikelihood provides the separation power for charge confusion.  
 1245 In figure 6, the distribution of the TRDLikelihood is shown.

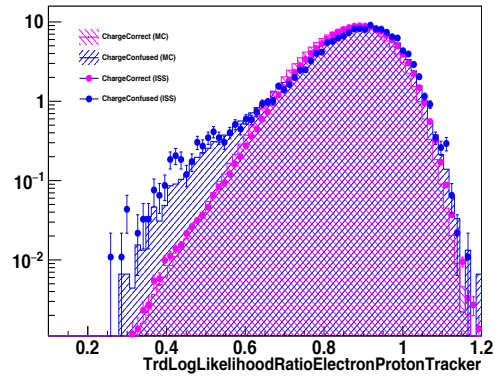


Figure 6: Distributions of TRDLikelihood in example rigidity bin of 330 to 525 GV. Histograms (magenta: charge correct; blue: charge confused) are taken from MC and points (magenta: charge correct; blue: charge confused) are from data.

## 1246 APPENDIX

### 1247 Acronyms

<b>ACC</b>	.....	Anti-Coincidence Counters
<b>AMS</b>	.....	Alpha Magnetic Spectrometer
<b>BDT</b>	.....	Boosted Decision Tree
<b>CALT</b>	.....	China Academy of Launch Vehicle Technology
<b>CC</b>	.....	Charge Confusion
<b>CR</b>	.....	Cosmic Rays
<b>ECAL</b>	.....	Electromagnetic Calorimeter
<b>GCR</b>	.....	Galactic Cosmic Rays
<b>GTB</b>	.....	Gradient Tree Boosting
<b>HCS</b>	.....	Heliospheric Current Sheet
<b>HMF</b>	.....	Heliospheric Magnetic Field
<b>HT</b>	.....	High Threshold
<b>IGRF</b>	.....	International Geomagnetic Reference Field
<b>ISM</b>	.....	Interstellar Medium
<b>ISS</b>	.....	International Space Station
<b>LEO</b>	.....	Low Earth Orbit
<b>LIS</b>	.....	Local Interstellar Spectra

<b>MHD</b>	.....	Magneto-Hydrodynamic
<b>NM</b>	.....	Neutron Monitor
<b>PWN</b>	.....	Pulsar Wind Nebula
<b>RICH</b>	.....	Ring-Imaging Cherenkov detector
<b>SAA</b>	.....	South Atlantic Anomaly
<b>SHT</b>	.....	Super High Threshold
<b>SNRs</b>	.....	Supernova Remnants
<b>SSN</b>	.....	Sunspot Number
<b>SVM</b>	.....	Support Vector Machine
<b>TOF</b>	.....	Time Of Flight
<b>TOI</b>	.....	Top-Of-Instrument
<b>TRD</b>	.....	Transition Radiation Detector
<b>TTCS</b>	.....	Tracker Thermal Cooling System

1248

1249

1250

# LIST OF FIGURES

1251	Figure 2.1	(a). Cosmic ray spectrum has a wide range in flux and energy [12] , the knee is at around 1 PeV and the ankle is at 4 EeV. (b). The fluxes of different components of cosmic rays follow a universal power law trend [13] . . . . .	4
1252			
1253			
1254	Figure 2.2	A good agreement of element abundances between the GCR and the solar system is shown [14] , except some differences like over-abundance of H and He in solar system, excess of Li, Be, B in GCR and others. . . . .	5
1255			
1256			
1257	Figure 2.3	a): Diagram of the heliosphere. Credit: NASA/Walt Feimer; b). Particle rate detected by Voyager 1 (from October 2011 through October 2012) [42] .	8
1258			
1259	Figure 2.4	Bottom figure: The cosmic rays (CR) intensity recorded by neutron monitor (NM) counts from four different stations (MCMD = McMurdo, NEWK = Newark, SOPO = South Pole, THUL = Thule). The vertical lines show the approximations of epochs of solar magnetic-field polarity reversals and qA is the solar polarity. Top figure: Monthly mean sunspot numbers (SSN) over the latest six solar cycles. The vertical lines show the beginning of each solar cycle. The figure is taken from [47] . . . . .	9
1260			
1261			
1262			
1263			
1264			
1265			
1266	Figure 2.5	The antiproton flux measured by BESS-Polar II [53] , PAMELA [7] , and AMS-02 [1] . . . . .	11
1267			
1268	Figure 3.1	a). AMS-01 test flight aboard Space Shuttle Discovery on the STS-91 mission in June 1998 [60] ; b). AMS-01 detector was installed in the support structure at Kennedy Space Center (NASA). credit: AMS-01 brochure . .	13
1269			
1270			
1271	Figure 3.2	AMS-02 detector mounted on the ISS S3 Upper Inboard Payload Attach Site. Image modified from [61] . . . . .	13
1272			
1273	Figure 3.3	Schematic view of AMS-02 experiment and its all sub-detectors. [63] . . .	14
1274	Figure 3.4	A overview of AMS-02 experiment operations flow in flight and ground [64]	15
1275	Figure 3.5	TRD final construction completed in RWTH Aachen University. [68] . .	16
1276	Figure 3.6	Illustration of TRD separation between electrons and protons [64] : the left figure shows the transition radiation emitted by positron while proton only left dEdX signal; the right figure shows an example of tube collected energy for 100 GeV protons and 20 GeV electrons . . . . .	16
1277			
1278			
1279			

1280	Figure 3.7	Seperation between the electrons and protons in TRDLikelihood estimator.	
1281		[64] . . . . .	17
1282	Figure 3.8	Preparing for the vibration test of the permanent magnet in China Academy	
1283		of Launch Vehicle Technology (CALT) [64] . . . . .	18
1284	Figure 3.9	Deviation of measured magnetic fields of the permanent magnet between	
1285		1997 and 2010 [64] . . . . .	19
1286	Figure 3.10	Drift of the electron-hole pair in silicon sensor produced by a charged par-	
1287		ticle. [64] . . . . .	20
1288	Figure 3.11	Tracker resolution comparison between 400 GeV protons beam test and MC	
1289		comparison. [64] . . . . .	21
1290	Figure 3.12	TOF planes arrangement in AMS-02 experiment, left is Upper TOF and	
1291		right is Lower TOF [78] . . . . .	22
1292	Figure 3.13	a). TOF Beta resolution as the function for particle charge. [78] ; b). TOF	
1293		charge distribution from proton (Z=1) to Zinc (Z=30). [78] . . . . .	23
1294	Figure 3.17	ECAL energy resolution from beam test data [89] . . . . .	23
1295	Figure 3.14	RICH PMT plane and expansion volume in the front and two radiators in	
1296		the behind. [81] . . . . .	24
1297	Figure 3.15	a). RICH beta resolution as the function for particle charge. [82] ; b).	
1298		RICH charge resolution as the function of particle charge. [82] . . . . .	25
1299	Figure 3.16	ECAL super layer structure and cell dimensions. [86] . . . . .	25
1300	Figure 3.18	Upper left: ACC counter system. Upper right: the principle of ACC ar-	
1301		rangement. Lower: Panel pair and PMTs connections. [93] . . . . .	25
1302	Figure 4.1	Four most important input variables used for training the charge confusion	
1303		estimator: a). <b>Chi2TrackerYAsymmetry</b> b). <b>InnerMaxSpanRigid-</b>	
1304		<b>ityMatching</b> c). <b>L1L9RigidityMatching</b> d). <b>RigidityAsymmetry</b> .	
1305		The points are collected data, and the histograms are proton MC simula-	
1306		tion. The pink is the distribution for the charge correct antiprotons, and	
1307		the blue is the distribution for the charge confused protons. . . . .	32
1308	Figure 4.2	The charge confusion estimator response on charge correct antiprotons (pink)	
1309		and charge confused protons (blue) in 147-175 GV . . . . .	34
1310	Figure 4.3	Seperation between the electrons and protons in TRDLikelihood estimator.	
1311		[64] . . . . .	35
1312	Figure 4.4	The ridigity-dependent lower edge of template fit range for 90% signal effi-	
1313		ciency. a). Lower edge for TOFBeta. b). Lower edge for TRDLikelihood.	
1314		. . . . .	37

1315	Figure 4.5	Example template fit in 3.64 to 4.02 GV in low rigidity range. a). 1/TOF-Beta projection. In this projection, the value is subtracted by the 1/Beta with the assumption of antiproton mass, so the distribution can be normalized to be around 0. b).TRDLikelihood projection . . . . .	38
1316			
1317			
1318			
1319	Figure 4.6	The antiproton numbers obtained from the template fit in low rigidity range	39
1320	Figure 4.7	The Chi2/dof of template fit in low rigidity range . . . . .	39
1321	Figure 4.8	Example template fit in 10.1 to 11 GV in intermediate rigidity range . . .	41
1322	Figure 4.9	The antiproton numbers obtained from the template fit in intermediate rigidity range . . . . .	41
1323			
1324	Figure 4.10	The Chi2/dof of template fit in intermediate rigidity range . . . . .	42
1325	Figure 4.11	Example template fit in 175 to 211 GV in high rigidity range. a). The charge confusion estimator projection b). The TRDLikelihood projection .	43
1326			
1327	Figure 4.12	The antiproton numbers obtained from the template fit in the high rigidity range. The fluctuation is due to either merged rigidity bins width or usage of different tracker patterns. . . . .	44
1328			
1329			
1330	Figure 4.13	The Chi2/dof of template fit in high rigidity range . . . . .	44
1331	Figure 4.14	Example template fit in 6.47 to 7.76 GV with data collected Jan.07.2020 to June.17.2020. . . . .	45
1332			
1333	Figure 4.15	Antiproton numbers from template fit results in 6.47 to 7.76 GV with six Bartel's Rotation time resolution . . . . .	46
1334			
1335	Figure 4.16	Chi2/dof of the template fits in 6.47 to 7.76 GV with six Bartel's Rotation time resolution . . . . .	46
1336			
1337	Figure 4.17	Proton to antiproton effective acceptance ratio in three rigidity ranges. . .	48
1338	Figure 4.18	Live time fraction vs. ISS position. The live time fraction in most area is above 0.9 while in SAA is extremely low. . . . .	49
1339			
1340	Figure 4.19	Measuring time as a function of live time fraction. In most of the measuring time, the live time fraction is above 0.9. . . . .	50
1341			
1342	Figure 4.20	Triggers as a function of particle over trigger ratio. For most triggers, each trigger fires around 0.11 particles . . . . .	50
1343			
1344	Figure 4.21	Illustration of Earth's magnetic field. Credit: Peter Reid, The University of Edinburgh . . . . .	51
1345			
1346	Figure 4.22	The Størmer rigidity cutoff used in this analysis as a function of ISS Position. The maximum of the cutoff is less than 30 GV. . . . .	52
1347			

1348	Figure 4.23	The measuring time obtained from the Størmer geomagnetic cutoff. After the quality cuts and live time fraction, the resulting total measuring time is around 2488 days. . . . .	52
1349			
1350			
1351	Figure 4.24	The comparison between the Størmer and IGRF cutoffs. The IGRF cutoff leads to lower measuring time . . . . .	53
1352			
1353	Figure 4.25	The proton trigger efficiency. . . . .	55
1354	Figure 4.26	The migration matrix for full span in high rigidity range. The X axis is the reconstructed rigidity from the Tracker, the Y axis is the true rigidity from the generated momentum in MC. . . . .	57
1355			
1356			
1357	Figure 4.27	The residual over unfolded number for full span in high rigidity range . . .	57
1358	Figure 4.28	The systematic error from acceptance . . . . .	59
1359	Figure 4.29	The template fit result in 2.15 to 2.4 GV with signal efficiency from 40%. a). The template fit result distribution as a function of signal efficiency. b). The template fit result histogram. The RMS of the histogram is used as the systematic error. . . . .	60
1360			
1361			
1362			
1363	Figure 4.31	Data/MC charge confusion level ratio. . . . .	60
1364	Figure 4.30	The systematic error from template fit range . . . . .	61
1365	Figure 4.32	The systematic error from charge confusion . . . . .	61
1366	Figure 4.33	The total systematic error . . . . .	62
1367	Figure 4.34	Systematic error of the antiproton to proton flux ratio in 1.92 to 2.4 GV in six Bartels Rotation time bin . . . . .	63
1368			
1369	Figure 5.1	The time-averaged antiproton to proton flux ratios in three rigidity ranges is shown. In the overlapping ranges, the results from different template fit methods are consistent with each other. The error bars are total errors calculated from the quadratic sum of statistical and systematic errors. . . .	65
1370			
1371			
1372			
1373	Figure 5.2	The final result of the time-averaged antiproton to proton flux ratio with the data taken from May 2011 to May 2021 in this analysis. The error bar is the total error calculated from the quadratic sum of statistical and systematic error. . . . .	65
1374			
1375			
1376			
1377	Figure 5.3	Comparison between the antiproton to proton flux ratio in this analysis and in Physics Report [107] , both of the two flux ratios use six and half years of data. The two results match with each other within the error bars. . . .	66
1378			
1379			



1380	Figure 5.4	The uncertainty breakdown of the time-averaged antiproton to proton flux ratio in this analysis. In the highest rigidity bin, the systematic uncertainty is dominated due to the charge confusion protons. In the low rigidity range, the statistical uncertainty and systematic uncertainty make similar contributions. . . . .	66
1381			
1382			
1383			
1384			
1385	Figure 5.5	Time-dependent antiproton to proton flux ratios for four of the 14 rigidity bins. The error bars in this figure are total errors, including statistical errors and systematic errors. Distinct time variation structures are visible in these ratios. . . . .	67
1386			
1387			
1388			
1389	Figure 5.6	Breakdown of the total uncertainty of the antiproton to proton flux ratio into a statistical and systematical part in 1.92 to 2.4 GV. . . . .	68
1390			
1391	Figure 5.7	Percentage of statistical uncertainty in total uncertainty of the antiproton to proton flux ratio in 1.92 - 2.4 GV. . . . .	69
1392			
1393	Figure 5.8	time-averaged antiproton to proton flux ratio (red) and 23 time-dependent antiproton to proton flux ratios in six Bartels rotations (green). The time-dependent results are changed around the time-averaged result. . . . .	70
1394			
1395			
1396	Figure 5.9	Time-averaged antiproton to proton flux ratio (red) and merged time-dependent antiproton to proton flux ratios in six Bartels rotations (green). The merged time-dependent result matches well with the time-averaged result. . . . .	70
1397			
1398			
1399	Figure 5.10	Comparison between antiproton to proton flux ratio (blue) and electron to positron flux ratio (red) in four rigidity bins: a). 1.92-2.4 GV b). 2.4-2.97 GV c). 4.43-5.37 GV d). 6.47-7.76 GV. The error bars are the total errors calculated from the quadratic sum of statistical errors and systematic errors. . . . .	73
1400			
1401			
1402			
1403	Figure 1	Distributions of a). RigidityAsymmetry b). L24L58RigidityMatching in example rigidity bin of 330 to 525 GV. Histograms (magenta: charge correct; blue: charge confused) are taken from MC and points (magenta: charge correct; blue: charge confused) are from data. . . . .	77
1404			
1405			
1406			
1407	Figure 2	Distributions of a). Log10Chi2TrackerX b). Log10Chi2TrackerY c). Log10Chi2TrackerXInner d). Log10Chi2TrackerYInner in example rigidity bin of 330 to 525 GV. Histograms (magenta: charge correct; blue: charge confused) are taken from MC and points (magenta: charge correct; blue: charge confused) are from data. . . . .	78
1408			
1409			
1410			
1411			
1412	Figure 3	Distributions of a). TrackerL9Charge b). TrackerL78Charge in example rigidity bin of 330 to 525 GV. Histograms (magenta: charge correct; blue: charge confused) are taken from MC and points (magenta: charge correct; blue: charge confused) are from data. . . . .	79
1413			
1414			
1415			

1416	Figure 4	Distributions of TrackerL58L24ChargeAsymmetry in example rigidity bin of 330 to 525 GV. Histograms (magenta: charge correct; blue: charge confused) are taken from MC and points (magenta: charge correct; blue: charge confused) are from data. . . . .	80
1417			
1418			
1419			
1420	Figure 5	Distributions of a). LowerTofCharge b). UpperTofCharge in example rigidity bin of 330 to 525 GV. Histograms (magenta: charge correct; blue: charge confused) are taken from MC and points (magenta: charge correct; blue: charge confused) are from data. . . . .	80
1421			
1422			
1423			
1424	Figure 6	Distributions of TRDLikelihood in example rigidity bin of 330 to 525 GV. Histograms (magenta: charge correct; blue: charge confused) are taken from MC and points (magenta: charge correct; blue: charge confused) are from data. . . . .	81
1425			
1426			
1427			

1428

1429

1430

# LIST OF TABLES

1431	TABLE 4.1	List of data taking quality cuts . . . . .	28
1432	TABLE 4.2	List of analysis data quality cuts . . . . .	29
1433	TABLE 4.3	List of quality cuts . . . . .	30
1434	TABLE 4.4	List of selections for templates . . . . .	37
1435	TABLE 4.5	List of selections for templates . . . . .	40

## BIBLIOGRAPHY

- 1436
- 1437 [1] M. Aguilar et al. (AMS Collaboration). Antiproton Flux, Antiproton-to-Proton Flux Ratio,  
1438 and Properties of Elementary Particle Fluxes in Primary Cosmic Rays Measured with the  
1439 Alpha Magnetic Spectrometer on the International Space Station. *Phys. Rev. Lett.*, 117:091103,  
1440 Aug 2016. DOI: [10.1103/PhysRevLett.117.091103](https://doi.org/10.1103/PhysRevLett.117.091103).
- 1441 [2] NobelPrize.org (Nobel Media AB). Victor F. Hess - Facts, 2022. URL:  
1442 <https://www.nobelprize.org/prizes/physics/1936/hess/facts>.
- 1443 [3] NobelPrize.org (Nobel Media AB). Carl D. Anderson - Facts, 2022. URL:  
1444 <https://www.nobelprize.org/prizes/physics/1936/anderson/facts>.
- 1445 [4] NobelPrize.org (Nobel Media AB). The Nobel Prize in Physics 1959, 2022. URL:  
1446 <https://www.nobelprize.org/prizes/physics/1959/summary>.
- 1447 [5] E. A. Bogomolov, N. D. Lubyanyaya, V. A. Romanov, S. V. Stepanov, and M. S. Shulakova. A  
1448 Stratospheric Magnetic Spectrometer Investigation of the Singly Charged Component Spectra  
1449 and Composition of the Primary and Secondary Cosmic Radiation. In *International Cosmic*  
1450 *Ray Conference*, volume 1, page 330, 1979.
- 1451 [6] R. L. Golden, S. Horan, B. G. Mauger, G. D. Badhwar, J. L. Lacy, S. A. Stephens, R. R.  
1452 Daniel, and J. E. Zipse. Evidence for the Existence of Cosmic-Ray Antiprotons. *Phys. Rev.*  
1453 *Lett.*, 43:1196–1199, Oct 1979. DOI: [10.1103/PhysRevLett.43.1196](https://doi.org/10.1103/PhysRevLett.43.1196).
- 1454 [7] O. Adriani et al. Measurement of the flux of primary cosmic ray antiprotons with energies of  
1455 60-MeV to 350-GeV in the PAMELA experiment. *Pisma Zh. Eksp. Teor. Fiz.*, 96:693–699,  
1456 2012. DOI: [10.1134/S002136401222002X](https://doi.org/10.1134/S002136401222002X).
- 1457 [8] Kenneth Greisen. End to the Cosmic-Ray Spectrum? *Phys. Rev. Lett.*, 16:748–750, Apr 1966.  
1458 DOI: [10.1103/PhysRevLett.16.748](https://doi.org/10.1103/PhysRevLett.16.748).
- 1459 [9] G. T. Zatsepin and V. A. Kuzmin. Upper Limit of the Spectrum of Cosmic Rays. *Sov-*  
1460 *iet Journal of Experimental and Theoretical Physics Letters*, 4:78, Aug 1966. URL:  
1461 <https://www.osti.gov/biblio/4515382>.
- 1462 [10] D. J. Bird et al. Detection of a Cosmic Ray with Measured Energy Well beyond the Expected  
1463 Spectral Cutoff due to Cosmic Microwave Radiation. *Astrophysical Journal*, 441:144, Mar  
1464 1995. DOI: [10.1086/175344](https://doi.org/10.1086/175344).
- 1465 [11] R. Abbasi et al. Indications of Intermediate-Scale Anisotropy of Cosmic Rays with Energy  
1466 Greater Than 57 EeV in the Northern Sky Measured with the Surface Detector of the Telescope  
1467 Array Experiment. *The Astrophysical Journal*, 790(2):L21, Jul 2014. DOI: [10.1088/2041-](https://doi.org/10.1088/2041-8205/790/2/L21)  
1468 [8205/790/2/L21](https://doi.org/10.1088/2041-8205/790/2/L21).
- 1469 [12] Alicia Lopez Oramas. Multi-year Campaign of the Gamma-Ray Binary LS I +61° 303 and  
1470 Search for VHE Emission from Gamma-Ray Binary Candidates with the MAGIC Telescopes.  
1471 PhD thesis, Universitat Autònoma de Barcelona, Apr 2015. DOI: [10.13140/RG.2.1.4140.4969](https://doi.org/10.13140/RG.2.1.4140.4969).
- 1472 [13] R. L. et al. (Particle Data Group) Workman. Review of Particle Physics. *PTEP*,  
1473 2022:p.083C01, 2022. DOI: [10.1093/ptep/ptac097](https://doi.org/10.1093/ptep/ptac097).

- 1474 [14] Alessandra Pacini. Cosmic rays: Bringing messages from the sky to the Earth’s surface. *Revista*  
1475 *Brasileira de Ensino de Física*, 39, Jan 2017. DOI: [10.1590/1806-9126-RBEF-2016-0168](https://doi.org/10.1590/1806-9126-RBEF-2016-0168).
- 1476 [15] W. Baade and F. Zwicky. Cosmic Rays from Super-novae. *Proceedings of the Na-*  
1477 *tional Academy of Sciences of the United States of America*, 20(5):259–263, 1934. URL:  
1478 <http://www.jstor.org/stable/86841>.
- 1479 [16] Massimo Turatto. *Classification of Supernovae*, pages 21–36. Springer Berlin Heidelberg,  
1480 Berlin, Heidelberg, 2003. DOI: [10.1007/3-540-45863-8\\_3](https://doi.org/10.1007/3-540-45863-8_3).
- 1481 [17] Stephen P. Reynolds. Supernova Remnants at High Energy. *Annual Review of Astronomy and*  
1482 *Astrophysics*, 46(1):89–126, 2008. DOI: [10.1146/annurev.astro.46.060407.145237](https://doi.org/10.1146/annurev.astro.46.060407.145237).
- 1483 [18] Malcolm S. Longair. High Energy Astrophysics. UK: Cambridge University Press, 2011. URL:  
1484 <https://ui.adsabs.harvard.edu/abs/2011hea..book.....L>.
- 1485 [19] ENRICO Fermi. On the Origin of the Cosmic Radiation. *Phys. Rev.*, 75:1169–1174, Apr 1949.  
1486 DOI: [10.1103/PhysRev.75.1169](https://doi.org/10.1103/PhysRev.75.1169).
- 1487 [20] T. Gold, F. G. Smith, and A. W. Wolfendale. Pulsars and the Origin of Cosmic Rays and  
1488 Discussion. *Philosophical Transactions of the Royal Society of London. Series A, Mathematical*  
1489 *and Physical Sciences*, 277(1270):453–461, 1975. URL: <http://www.jstor.org/stable/74493>.
- 1490 [21] Bednarek, W. and Bartosik, M. Cosmic rays from Galactic pulsars. *Astronomy & Astrophysics*,  
1491 423(2):405–413, 2004. DOI: [10.1051/0004-6361:20047005](https://doi.org/10.1051/0004-6361:20047005).
- 1492 [22] J Arons. Pulsar wind nebulae as cosmic pevatrons: A current sheet’s tale. *Space Sci Rev*,  
1493 173:341–367, 2012. DOI: [10.1007/s11214-012-9885-1](https://doi.org/10.1007/s11214-012-9885-1).
- 1494 [23] A. R. Bell. Cosmic ray acceleration in pulsar-driven supernova remnants. *Monthly Notices of*  
1495 *the Royal Astronomical Society*, 257(3):493–500, Aug 1992. DOI: [10.1093/mnras/257.3.493](https://doi.org/10.1093/mnras/257.3.493).
- 1496 [24] Dan Hooper, Pasquale Blasi, and Pasquale Dario Serpico. Pulsars as the sources of high energy  
1497 cosmic ray positrons. *Journal of Cosmology and Astroparticle Physics*, 2009(01):025, Jan 2009.  
1498 DOI: [10.1088/1475-7516/2009/01/025](https://doi.org/10.1088/1475-7516/2009/01/025).
- 1499 [25] R. Cowsik. Positrons and Antiprotons in Galactic Cosmic Rays. *Annual Review of Nuclear*  
1500 *and Particle Science*, 66(1):297–319, 2016. DOI: [10.1146/annurev-nucl-102115-044851](https://doi.org/10.1146/annurev-nucl-102115-044851).
- 1501 [26] V Bresci, E Amato, P Blasi, and G Morlino. Effects of re-acceleration and source gram-  
1502 mage on secondary cosmic rays spectra. *Monthly Notices of the Royal Astronomical Society*,  
1503 488(2):2068–2078, 07 2019. DOI: [10.1093/mnras/stz1806](https://doi.org/10.1093/mnras/stz1806).
- 1504 [27] Ilias Cholis, Tim Linden, and Dan Hooper. A robust excess in the cosmic-ray antiproton  
1505 spectrum: Implications for annihilating dark matter. *Phys. Rev. D*, 99:103026, May 2019.  
1506 DOI: [10.1103/PhysRevD.99.103026](https://doi.org/10.1103/PhysRevD.99.103026).
- 1507 [28] Jan Heisig. Cosmic-ray antiprotons in the ams-02 era: A sensitive probe of dark matter.  
1508 *Modern Physics Letters A*, 36(05):2130003, 2021. DOI: [10.1142/S0217732321300032](https://doi.org/10.1142/S0217732321300032).
- 1509 [29] Martin Wolfgang Winkler. Cosmic ray antiprotons at high energies. *Journal of Cosmology and*

- 1510 *Astroparticle Physics*, 2017(02):048–048, Feb 2017. DOI: [10.1088/1475-7516/2017/02/048](https://doi.org/10.1088/1475-7516/2017/02/048).
- 1511 [30] Rolf Kappl and Martin Wolfgang Winkler. The cosmic ray antiproton background for AMS-  
1512 02. *Journal of Cosmology and Astroparticle Physics*, 2014(09):051–051, Sep 2014. DOI:  
1513 [10.1088/1475-7516/2014/09/051](https://doi.org/10.1088/1475-7516/2014/09/051).
- 1514 [31] Ming-Yang Cui, Qiang Yuan, Yue-Lin Sming Tsai, and Yi-Zhong Fan. Possible dark matter  
1515 annihilation signal in the ams-02 antiproton data. *Phys. Rev. Lett.*, 118:191101, May 2017.  
1516 DOI: [10.1103/PhysRevLett.118.191101](https://doi.org/10.1103/PhysRevLett.118.191101).
- 1517 [32] Andrew W. Strong, Igor V. Moskalenko, and Vladimir S. Ptuskin. Cosmic-Ray Propagation  
1518 and Interactions in the Galaxy. *Annual Review of Nuclear and Particle Science*, 57(1):285–327,  
1519 2007. DOI: [10.1146/annurev.nucl.57.090506.123011](https://doi.org/10.1146/annurev.nucl.57.090506.123011).
- 1520 [33] Igor V. Moskalenko. Galprop: modeling cosmic ray propagation and associated interstellar  
1521 emissions, 2011. DOI: [10.48550/ARXIV.1105.4921](https://doi.org/10.48550/ARXIV.1105.4921).
- 1522 [34] David Maurin. usine: Semi-analytical models for Galactic cosmic-ray propagation. *Computer  
1523 Physics Communications*, 247:106942, 2020. DOI: [10.1016/j.cpc.2019.106942](https://doi.org/10.1016/j.cpc.2019.106942).
- 1524 [35] Carmelo Evoli, Daniele Gaggero, Andrea Vittino, Giuseppe Di Bernardo, Mattia Di Mauro,  
1525 Arianna Ligorini, Piero Ullio, and Dario Grasso. Cosmic-ray propagation with DRAGON2:  
1526 I. numerical solver and astrophysical ingredients. *Journal of Cosmology and Astroparticle  
1527 Physics*, 2017(02):015–015, Feb 2017. DOI: [10.1088/1475-7516/2017/02/015](https://doi.org/10.1088/1475-7516/2017/02/015).
- 1528 [36] V. S. Ptuskin, O. N. Strelnikova, and L. G. Sveshnikova. On leaky-box approximation to  
1529 GALPROP. *Astropart. Phys.*, 31:284–289, 2009. DOI: [10.1016/j.astropartphys.2009.02.004](https://doi.org/10.1016/j.astropartphys.2009.02.004).
- 1530 [37] E. N. Parker. Dynamics of the Interplanetary Gas and Magnetic Fields. *Astrophysical Journal*,  
1531 128:664, Nov 1958. DOI: [10.1086/146579](https://doi.org/10.1086/146579).
- 1532 [38] Christopher T. Russell. The Solar Wind and Magnetospheric Dynamics. In *Correlated Inter-  
1533 planetary and Magnetospheric Observations*, pages 3–47, Dordrecht, 1974. Springer Nether-  
1534 lands. DOI: [10.1007/978-94-010-2172-2\\_1](https://doi.org/10.1007/978-94-010-2172-2_1).
- 1535 [39] M.J. Owens and R.J. Forsyth. The Heliospheric Magnetic Field. *Living Rev. Sol. Phys.*, 10,  
1536 Nov 2013. DOI: [10.12942/lrsp-2013-5](https://doi.org/10.12942/lrsp-2013-5).
- 1537 [40] A. J. Dessler. Solar wind and interplanetary magnetic field. *Reviews of Geophysics*, 5(1):1–41,  
1538 1967. DOI: [10.1029/RG005i001p00001](https://doi.org/10.1029/RG005i001p00001).
- 1539 [41] R Cowen. Voyager 1 has reached interstellar space. *Nature*, 2013. DOI: [10.1038/nature.2013.13735](https://doi.org/10.1038/nature.2013.13735).
- 1541 [42] NASA. Solar wind at voyager 1, 2012. Retrieved 16:20, July 20, 2022 from:  
1542 [https://commons.wikimedia.org/wiki/File:Solar\\_wind\\_at\\_Voyager\\_1.png](https://commons.wikimedia.org/wiki/File:Solar_wind_at_Voyager_1.png).
- 1543 [43] David H. Hathaway. The Solar Cycle. *Living Reviews in Solar Physics*, 7(1):1, Dec 2010. DOI:  
1544 [10.12942/lrsp-2010-1](https://doi.org/10.12942/lrsp-2010-1).
- 1545 [44] Carsten Jorgensen, Christoffer Karoff, Senthamizh Pavai Valliappan, and Rainer Arlt. Chris-

- 1546 tian Horrebow's Sunspot Observations – I. Life and Published Writings. *Solar Physics*, Jun  
1547 2019. DOI: [10.1007/s11207-019-1465-z](https://doi.org/10.1007/s11207-019-1465-z).
- 1548 [45] Christoffer Karoff, Carsten Jorgensen, Senthamizh Pavai Valliappan, and Rainer Arlt. Chris-  
1549 tian Horrebow's Sunspot Observations – II. Construction of a Record of Sunspot Positions.  
1550 *Solar Physics*, 294, Jun 2019. DOI: [10.1007/s11207-019-1466-y](https://doi.org/10.1007/s11207-019-1466-y).
- 1551 [46] Gleeson.L and Axford.W. Solar Modulation of Galactic Cosmic Rays. *Astrophysical Journal*,  
1552 154:1011, Dec 1968. DOI: [10.1086/149822](https://doi.org/10.1086/149822).
- 1553 [47] Eddie Ross and William J. Chaplin. The behaviour of galactic cosmic ray intensity during  
1554 solar activity cycle 24. *Solar Physics*, 294(1):8, Jan 2019. DOI: [10.1007/s11207-019-1397-7](https://doi.org/10.1007/s11207-019-1397-7).
- 1555 [48] M. Aguilar et al. (AMS Collaboration). Observation of complex time structures in the cosmic-  
1556 ray electron and positron fluxes with the alpha magnetic spectrometer on the international  
1557 space station. *Phys. Rev. Lett.*, 121:051102, Jul 2018. DOI: [10.1103/PhysRevLett.121.051102](https://doi.org/10.1103/PhysRevLett.121.051102).
- 1558 [49] K. Anraku et al. Balloon borne experiment using a superconducting solenoidal  
1559 magnet spectrometer. In *KEK-PREPRINT-94-40*, 6 1994. URL: [https://lib-  
1560 extopc.kek.jp/preprints/PDF/1994/9427/9427040.pdf](https://lib-extopc.kek.jp/preprints/PDF/1994/9427/9427040.pdf).
- 1561 [50] M. Nozaki. BESS-Polar. *Nuclear Instruments and Methods in Physics Research*  
1562 *Section B: Beam Interactions with Materials and Atoms*, 214:110–115, 2004. DOI:  
1563 [10.1016/j.nimb.2003.08.005](https://doi.org/10.1016/j.nimb.2003.08.005).
- 1564 [51] T. Yoshida, A. Yamamoto, and J. et al. Mitchell. Bess-polar experiment. *Life sciences and*  
1565 *space research*, 33(10):1755–1762, 2004. DOI: [10.1016/j.asr.2003.05.017](https://doi.org/10.1016/j.asr.2003.05.017).
- 1566 [52] K. Abe et al. Measurement of the cosmic-ray low-energy antiproton spectrum with  
1567 the first BESS-Polar Antarctic flight. *Physics Letters B*, 670(2):103–108, 2008. DOI:  
1568 [10.1016/j.physletb.2008.10.053](https://doi.org/10.1016/j.physletb.2008.10.053).
- 1569 [53] K. Abe et al. Measurement of the Cosmic-Ray Antiproton Spectrum at Solar Minimum with a  
1570 Long-Duration Balloon Flight over Antarctica. *Phys. Rev. Lett.*, 108:051102, Jan 2012. DOI:  
1571 [10.1103/PhysRevLett.108.051102](https://doi.org/10.1103/PhysRevLett.108.051102).
- 1572 [54] A M Galper et al. The PAMELA experiment: a decade of Cosmic Ray Physics in space. *Journal*  
1573 *of Physics: Conference Series*, 798:012033, Jan 2017. DOI: [10.1088/1742-6596/798/1/012033](https://doi.org/10.1088/1742-6596/798/1/012033).
- 1574 [55] O. Adriani et al. (PAMELA Collaboration). New Measurement of the Antiproton-to-Proton  
1575 Flux Ratio up to 100 GeV in the Cosmic Radiation. *Phys. Rev. Lett.*, 102:051101, Feb 2009.  
1576 DOI: [10.1103/PhysRevLett.102.051101](https://doi.org/10.1103/PhysRevLett.102.051101).
- 1577 [56] O. Adriani et al. (PAMELA Collaboration). PAMELA Results on the Cosmic-Ray Antiproton  
1578 Flux from 60 MeV to 180 GeV in Kinetic Energy. *Phys. Rev. Lett.*, 105:121101, Sep 2010.  
1579 DOI: [10.1103/PhysRevLett.105.121101](https://doi.org/10.1103/PhysRevLett.105.121101).
- 1580 [57] S. et al. Ahlen. An antimatter spectrometer in space. *Nuclear Instruments and Methods in*  
1581 *Physics Research Section A: Accelerators, Spectrometers, Detectors and Associated Equipment*,  
1582 350(1):351–367, 1994. DOI: [10.1016/0168-9002\(94\)91184-3](https://doi.org/10.1016/0168-9002(94)91184-3).

- [58] Roberto Battiston. The antimatter spectrometer (AMS-02): A particle physics detector in space. *Nuclear Instruments and Methods in Physics Research Section A: Accelerators, Spectrometers, Detectors and Associated Equipment*, 588(1):227–234, 2008. DOI: [10.1016/j.nima.2008.01.044](https://doi.org/10.1016/j.nima.2008.01.044).
- [59] M Aguilar et al. The Alpha Magnetic Spectrometer (AMS) on the International Space Station: Part I - results from the test flight on the space shuttle. *Physics Reports*, 366(6):331–405, 2002. DOI: [10.1016/S0370-1573\(02\)00013-3](https://doi.org/10.1016/S0370-1573(02)00013-3).
- [60] Roskosmos. STS-91 PLB, 1998. Retrieved 16:20, July 20, 2022 from: [https://commons.wikimedia.org/wiki/File:STS-91\\_PLB.jpg](https://commons.wikimedia.org/wiki/File:STS-91_PLB.jpg).
- [61] NASA/Crew-2. View of the ISS taken during crew-2 flyaround (iss066-e-081311), 2021. Retrieved 16:20, July 20, 2022 from: [https://commons.wikimedia.org/wiki/File:View\\_of\\_the\\_ISS\\_taken\\_during\\_Crew-2\\_flyaround\\_\(ISS066-E-081311\).jpg](https://commons.wikimedia.org/wiki/File:View_of_the_ISS_taken_during_Crew-2_flyaround_(ISS066-E-081311).jpg).
- [62] Zoe Budrikis. A decade of AMS-02. *Nature Reviews Physics*, 3(5):308–308, Jan 2021. DOI: [10.1038/s42254-021-00320-7](https://doi.org/10.1038/s42254-021-00320-7).
- [63] Fabian Machate. *Study for large acceptance electron analysis with the Alpha Magnetic Spectrometer on the International Space Station*. Dissertation, RWTH Aachen University, Aachen, 2021. DOI: [10.18154/RWTH-2021-09976](https://doi.org/10.18154/RWTH-2021-09976).
- [64] AMS Collaboration. The Alpha Magnetic Spectrometer on the International Space Station, 2022. URL: <https://ams02.space>.
- [65] V. L. Ginzburg and I. M. Frank. Radiation of a uniformly moving electron due to its transition from one medium into another. *J. Phys. (USSR)*, 9:353–362, 1945.
- [66] M. Heil et al. Operations and Alignment of the AMS-02 Transition Radiation Detector. In *33rd International Cosmic Ray Conference*, page 1232, 2013. URL: <https://galprop.stanford.edu/elibrary/icrc/2013/papers/icrc2013-1232.pdf>.
- [67] T. Siedenburger. The AMS TRD. A gasdetector designed for operation in space. *Nuclear Physics B - Proceedings Supplements*, 150:30–33, 2006. DOI: [10.1016/j.nuclphysbps.2004.06.001](https://doi.org/10.1016/j.nuclphysbps.2004.06.001).
- [68] Thomas Kirn. The AMS-02 TRD on the international space station. *Nuclear Instruments and Methods in Physics Research Section A: Accelerators, Spectrometers, Detectors and Associated Equipment*, 706:43–47, 2013. DOI: [10.1016/j.nima.2012.05.010](https://doi.org/10.1016/j.nima.2012.05.010).
- [69] Jerzy Neyman, Egon Sharpe Pearson, and Karl Pearson. IX. On the problem of the most efficient tests of statistical hypotheses. *Philosophical Transactions of the Royal Society of London. Series A, Containing Papers of a Mathematical or Physical Character*, 231(694-706):289–337, 1933. DOI: [10.1098/rsta.1933.0009](https://doi.org/10.1098/rsta.1933.0009).
- [70] B. Blau, S.M. Harrison, H. Hofer, S.R. Milward, J.S.H. Ross, S.C.C. Ting, J. Ulbricht, and G. Viertel. The superconducting magnet of ams-02. *Nuclear Physics B - Proceedings Supplements*, 113(1):125–132, 2002. DOI: [10.1016/S0920-5632\(02\)01831-5](https://doi.org/10.1016/S0920-5632(02)01831-5).
- [71] K. Lubelsmeyer et al. Upgrade of the Alpha Magnetic Spectrometer (AMS-02) for long term



- operation on the International Space Station (ISS). *Nuclear Instruments and Methods in Physics Research Section A: Accelerators, Spectrometers, Detectors and Associated Equipment*, 654(1):639–648, 2011. DOI: [10.1016/j.nima.2011.06.051](https://doi.org/10.1016/j.nima.2011.06.051).
- [72] Pierre Erwan Saouter. Operation and Performance of AMS-02 Silicon Tracker. *PoS, Vertex2014:028*, 2015. DOI: [10.22323/1.227.0028](https://doi.org/10.22323/1.227.0028).
- [73] Sadakazu Haino. Performance of the AMS-02 silicon tracker in the ISS mission. *Nucl. Instrum. Meth. A*, 699:221–224, 2013. DOI: [10.1016/j.nima.2012.05.060](https://doi.org/10.1016/j.nima.2012.05.060).
- [74] G. Ambrosi et al. Alignment of the AMS-02 Silicon Tracker. In *33rd International Cosmic Ray Conference*, page 1260, 2013. URL: <https://ui.adsabs.harvard.edu/abs/2013ICRC...33..570A>.
- [75] B. Alpat et al. The internal alignment and position resolution of the ams-02 silicon tracker determined with cosmic-ray muons. *Nuclear Instruments and Methods in Physics Research Section A: Accelerators, Spectrometers, Detectors and Associated Equipment*, 613(2):207–217, 2010. DOI: [10.1016/j.nima.2009.11.065](https://doi.org/10.1016/j.nima.2009.11.065).
- [76] V. Bindi et al. Calibration and performance of the AMS-02 time of flight detector in space. *Nucl. Instrum. Meth. A*, 743:22–29, 2014. DOI: [10.1016/j.nima.2014.01.002](https://doi.org/10.1016/j.nima.2014.01.002).
- [77] V. Bindi, A. Contin, N. Masi, A. Oliva, F. Palmonari, L. Quadrani, and A. Tiseni. The time of flight detector of the AMS-02 experiment on the international space station. *Nucl. Instrum. Meth. A*, 718:478–480, 2013. DOI: [10.1016/j.nima.2012.11.061](https://doi.org/10.1016/j.nima.2012.11.061).
- [78] V. Bindi, E. Choumilov, A. Contin, N. Masi, A. Oliva, F. Palmonari, L. Quadrani, and Q. Yan. The AMS-02 Time of Flight (TOF) System: Construction and Overall Performances in Space. In *International Cosmic Ray Conference*, volume 33 of *International Cosmic Ray Conference*, page 2298, Jan 2013. URL: <https://ui.adsabs.harvard.edu/abs/2013ICRC...33.2298B>.
- [79] Hu Liu, J. Casaus, F. Giovacchini, A. Oliva, and X. Xia. The RICH detector of AMS-02: 5 years of operation in space. *Nucl. Instrum. Meth. A*, 876:5–8, 2017. DOI: [10.1016/j.nima.2016.12.011](https://doi.org/10.1016/j.nima.2016.12.011).
- [80] R. Pereira. The AMS-02 RICH detector: Performance during ground-based data taking at CERN. *Nucl. Instrum. Meth. A*, 639:37–41, 2011. DOI: [10.1016/j.nima.2010.09.036](https://doi.org/10.1016/j.nima.2010.09.036).
- [81] F. Giovacchini, J. Casaus, and A. Oliva. The AMS-02 RICH detector: Status and physics results. *Nuclear Instruments and Methods in Physics Research Section A: Accelerators, Spectrometers, Detectors and Associated Equipment*, 952:161797, 2020. DOI: [10.1016/j.nima.2019.01.024](https://doi.org/10.1016/j.nima.2019.01.024).
- [82] F. Giovacchini. Performance in space of the AMS-02 RICH detector. *Nuclear Instruments and Methods in Physics Research Section A: Accelerators, Spectrometers, Detectors and Associated Equipment*, 766:57–60, 2014. DOI: [10.1016/j.nima.2014.04.036](https://doi.org/10.1016/j.nima.2014.04.036).
- [83] Sylvie Rosier-Lees. Performance of the AMS02 electromagnetic calorimeter in space. *J. Phys. Conf. Ser.*, 404:012034, 2012. DOI: [10.1088/1742-6596/404/1/012034](https://doi.org/10.1088/1742-6596/404/1/012034).
- [84] M. Vecchi et al. The electromagnetic calorimeter of the AMS-02 experiment. In *Semaine de l’Astrophysique Française (SF2A 2012)*, Nice, France, Jun 2012. URL: <http://hal.in2p3.fr/in2p3-00745677>.

- 1659 [85] C. Adloff et al. The AMS-02 lead-scintillating fibres Electromagnetic Calorimeter. *Nucl.*  
1660 *Instrum. Meth. A*, 714:147–154, 2013. DOI: [10.1016/j.nima.2013.02.020](https://doi.org/10.1016/j.nima.2013.02.020).
- 1661 [86] Marco Incagli. Performance of the AMS-02 Electromagnetic Calorimeter in Space. *PoS,*  
1662 *TIPP2014:025*, 2014. DOI: [10.22323/1.213.0025](https://doi.org/10.22323/1.213.0025).
- 1663 [87] Manuela Vecchi, Kaiyuan Wu, and Yuan-Hann Chang. A 3-dimensional electromagnetic  
1664 shower characterization and its application to AMS-02 pointing capability. In *33rd Inter-*  
1665 *national Cosmic Ray Conference*, page 0653, 2013.
- 1666 [88] Stefano Di Falco. Results of 2007 test beam of AMS-02 Electromagnetic Calorimeter. *Adv.*  
1667 *Space Res.*, 45:112–122, 2010. DOI: [10.1016/j.asr.2009.08.005](https://doi.org/10.1016/j.asr.2009.08.005).
- 1668 [89] G Gallucci and (for the AMS-02 ECAL group). Performance of the AMS-02 Electromagnetic  
1669 Calorimeter in Space. *Journal of Physics: Conference Series*, 587:012028, Feb 2015. DOI:  
1670 [10.1088/1742-6596/587/1/012028](https://doi.org/10.1088/1742-6596/587/1/012028).
- 1671 [90] Ph. von Doetinchem, W. Karpinski, Th. Kirn, K. Luebelsmeyer, St. Schael, and M. Wlochal.  
1672 The AMS-02 Anticoincidence Counter. *Nucl. Phys. B Proc. Suppl.*, 197:15–18, 2009. DOI:  
1673 [10.1016/j.nuclphysbps.2009.10.025](https://doi.org/10.1016/j.nuclphysbps.2009.10.025).
- 1674 [91] T. Bruch and W. Wallraff. The Anti-Coincidence Counter shield of the AMS tracker. *Nucl.*  
1675 *Instrum. Meth. A*, 572:505–507, 2007. DOI: [10.1016/j.nima.2006.10.376](https://doi.org/10.1016/j.nima.2006.10.376).
- 1676 [92] A. Basili, V. Bindi, D. Casadei, G. Castellini, A. Contin, A. Kounine, M. Lolli, F. Palmonari,  
1677 and L. Quadrani. The TOF-ACC flight electronics for the fast trigger and time of flight  
1678 of the AMS-02 cosmic ray spectrometer. *Nucl. Instrum. Meth. A*, 707:99–113, 2013. DOI:  
1679 [10.1016/j.nima.2012.12.089](https://doi.org/10.1016/j.nima.2012.12.089).
- 1680 [93] Ph. von Doetinchem, Th. Kirn, K. Luebelsmeyer, and St. Schael. The Anticoincidence Counter  
1681 System of AMS-02, 2009. DOI: [10.48550/ARXIV.0906.1068](https://doi.org/10.48550/ARXIV.0906.1068).
- 1682 [94] Rene Brun and Fons Rademakers. Root - An object oriented data analysis framework. *Nuclear*  
1683 *Instruments and Methods in Physics Research Section A: Accelerators, Spectrometers, Detec-*  
1684 *tors and Associated Equipment*, 389(1):81–86, 1997. DOI: [10.1016/S0168-9002\(97\)00048-X](https://doi.org/10.1016/S0168-9002(97)00048-X).
- 1685 [95] Bastian Beischer. *Measurement of high energy gamma rays from 200 MeV to 1 TeV with the*  
1686 *Alpha Magnetic Spectrometer on the International Space Station*. Dissertation, RWTH Aachen  
1687 University, Aachen, 2020. DOI: [10.18154/RWTH-2020-06535](https://doi.org/10.18154/RWTH-2020-06535).
- 1688 [96] M. Aguilar et al. (AMS Collaboration). Precision Measurement of the Proton Flux in Primary  
1689 Cosmic Rays from Rigidity 1 GV to 1.8 TV with the Alpha Magnetic Spectrometer on the  
1690 International Space Station. *Phys. Rev. Lett.*, 114:171103, Apr 2015. DOI: [10.1103/Phys-](https://doi.org/10.1103/PhysRevLett.114.171103)  
1691 [RevLett.114.171103](https://doi.org/10.1103/PhysRevLett.114.171103).
- 1692 [97] J. Bartels. Twenty-seven day recurrences in terrestrial-magnetic and solar activity, 1923-  
1693 1933. *Terrestrial Magnetism and Atmospheric Electricity*, 39(3):201–202a, 1934. DOI:  
1694 [10.1029/TE039i003p00201](https://doi.org/10.1029/TE039i003p00201).
- 1695 [98] S. Agostinelli et al. GEANT4—a simulation toolkit. *Nucl. Instrum. Meth. A*, 506:250–303,  
1696 2003. DOI: [10.1016/S0168-9002\(03\)01368-8](https://doi.org/10.1016/S0168-9002(03)01368-8).

- 1697 [99] J. Allison et al. Recent developments in Geant4. *Nucl. Instrum. Meth. A*, 835:186–225, 2016.  
1698 DOI: [10.1016/j.nima.2016.06.125](https://doi.org/10.1016/j.nima.2016.06.125).
- 1699 [100] Paolo Zuccon. AMS-02 Track reconstruction and rigidity measurement. In *33rd International Cosmic Ray Conference*, page 1064, 2013. URL: <https://s3.cern.ch/inspire-prod-files-7/71c48c76263c1f7bee2621c779ba3320>.  
1700  
1701
- 1702 [101] Helge Voss, Andreas Hocker, Jorg Stelzer, and Fredrik Tegenfeldt. TMVA, the toolkit for  
1703 multivariate data analysis with ROOT. In *XI International Workshop on Advanced Computing  
1704 and Analysis Techniques in Physics Research*, volume 50, page 040. SISSA Medialab, 2009.  
1705 DOI: [10.22323/1.050.0040](https://doi.org/10.22323/1.050.0040).
- 1706 [102] J.D. Sullivan. Geometric factor and directional response of single and multi-element par-  
1707 ticle telescopes. *Nuclear Instruments and Methods*, 95(1):5–11, 1971. DOI: [10.1016/0029-554X\(71\)90033-4](https://doi.org/10.1016/0029-554X(71)90033-4).  
1708
- 1709 [103] Nikolas Zimmermann. *Precision measurement of the cosmic-ray electron and positron fluxes as  
1710 a function of time and energy with the Alpha Magnetic Spectrometer on the International Space  
1711 Station*. Dissertatison, RWTH Aachen University, Aachen, 2020. DOI: [10.18154/RWTH-2020-02650](https://doi.org/10.18154/RWTH-2020-02650).  
1712
- 1713 [104] Carl Stormer. The polar aurora. *Quarterly Journal of the Royal Meteorological Society*,  
1714 82(351):115–115, 1956. DOI: [10.1002/qj.49708235123](https://doi.org/10.1002/qj.49708235123).
- 1715 [105] G. D’Agostini. A multidimensional unfolding method based on Bayes’ theorem. *Nuclear In-  
1716 struments and Methods in Physics Research Section A: Accelerators, Spectrometers, Detectors  
1717 and Associated Equipment*, 362(2):487–498, 1995. DOI: [10.1016/0168-9002\(95\)00274-X](https://doi.org/10.1016/0168-9002(95)00274-X).
- 1718 [106] Tim Adye. Unfolding algorithms and tests using RooUnfold. In *PHYSTAT 2011*, pages 313–  
1719 318, Geneva, 2011. CERN. DOI: [10.5170/CERN-2011-006.313](https://doi.org/10.5170/CERN-2011-006.313).
- 1720 [107] M. Aguilar et al. (AMS Collaboration). The Alpha Magnetic Spectrometer (AMS) on the  
1721 international space station: Part II – Results from the first seven years. *Physics Reports*,  
1722 894:1–116, 2021. DOI: [10.1016/j.physrep.2020.09.003](https://doi.org/10.1016/j.physrep.2020.09.003).
- 1723 [108] Marius S. Potgieter, O. P. M. Aslam, Driaan Bisschoff, and Donald Ngobeni. A perspec-  
1724 tive on the solar modulation of cosmic anti-matter. *Physics*, 3(4):1190–1225, 2021. DOI:  
1725 [10.3390/physics3040076](https://doi.org/10.3390/physics3040076).
- 1726 [109] John W. Bieber, R. A. Burger, Ralph Engel, Thomas K. Gaisser, Stefan Roesler, and Todor  
1727 Stanev. Antiprotons at solar maximum. *Phys. Rev. Lett.*, 83:674–677, Jul 1999. DOI:  
1728 [10.1103/PhysRevLett.83.674](https://doi.org/10.1103/PhysRevLett.83.674).
- 1729 [110] S. Schael et al. AMS-100: The next generation magnetic spectrometer in space - An interna-  
1730 tional science platform for physics and astrophysics at Lagrange point 2. *Nuclear Instruments  
1731 and Methods in Physics Research Section A: Accelerators, Spectrometers, Detectors and As-  
1732 sociated Equipment*, 944:162561, 2019. DOI: [10.1016/j.nima.2019.162561](https://doi.org/10.1016/j.nima.2019.162561).

# Acknowledgements

First, I would like to thank Prof. Dr. Stefan Schael to give me the opportunity to work in his institute and also as a member of the AMS-02 collaboration. During the last few years, I can always benefit from his supervision and guidance. His passion for Physics and enthusiasm really inspire me. Also, I learn a lot from his ambitions to push things forward.

I would also like to thank Prof. Dr. Christopher Wiebusch for agreeing to be my second supervisor for the thesis.

Second, I would also like to thank Prof. Samuel Ting, the PI of the whole AMS-02 experiment. Without his effort in the last decades, the AMS-02 project would not come true. His spirit of never giving up will inspire me in the future. In addition, I admire his concentration and perseverance shown in his career.

Many friends and colleagues helped me a lot during my PhD time in Aachen. Special thanks to Robin Sonnabend who helped me from zero ground when I was a beginner in AMS. He is always patient to teach me and answer stupid questions. I would like to thank Dr. Henning Gast. As the actual host in the Aachen analysis group, he put a lot of effort to support the Aachen data analysis.

During my PhD study in the institute, many friends and colleagues make my working time pleasant: Dr. Nikolas Zimmermann, Dr. Bastian Beischer, Dr. Fabian Machate, Dr. Nikolay Nikonov, Dr. Leila Ali Cavasonza, Dr. Sofia Chouridou, Manbing Li, Emiliano Rampi, Yasaman Najafi. I can always learn a lot from discussions with you, and the time I spent with you guys has already been a precious memory for me.

I would like to thank again to Dr. Henning Gast and Dr. Sofia Chouridou who did proofreadings for this thesis. Many thanks for your time and valuable comments.

I would like to thank Georg Schwering, Natalie Driessen, Tanja Bingler and Gina Wilden for their support work in the administration branch of the institute. As a foreigner working in Aachen, I was guided by them in almost every step of my PhD program.

During my shift at CERN, many friends and colleagues there make my stay enjoyable. I would like to thank Dr. Mike Capell, Dr. Zhili Weng, Dr. Weiwei Xu, Dr. Valery Zhukov, Dr. Youmin Yu, Dr. Baosong Shan, Dr. Yi Jia, Dr. XiaoTing Qin, and so many people. The talks at POCC can

1761 always make the time delightful.

1762 Last but foremost, I would like to thank my family. The forever love and encouragement are the  
1763 sources of power for me that support me all the time. The thesis wouldn't be done without your  
1764 sacrifice behind.